

# On-demand microfluidic droplet pinching and splitting under local confinement gradients

Margaux Kerdraon,<sup>1</sup> Albane Théry,<sup>1,2</sup> Marc Pascual,<sup>1</sup> Stéphanie Descroix,<sup>3</sup> and Marie-Caroline Jullien<sup>4,\*</sup>

<sup>1</sup>*Gulliver CNRS UMR 7083, PSL Research University, ESPCI Paris, 10 rue Vauquelin, 75005 Paris, France*

<sup>2</sup>*Department of Mathematics, University of Pennsylvania, 19014 Philadelphia, Pennsylvania, USA*

<sup>3</sup>*Institut Curie, CNRS UMR168, Laboratoire Physico Chimie Curie,*

*Institut Pierre-Gilles de Gennes, PSL Research University, 75005 Paris, France*

<sup>4</sup>*Université Rennes, CNRS, IPR (Institut de Physique de Rennes) - UMR 6251, F-35000 Rennes, France*

(Dated: November 1, 2024)

We report the pinching of an elongated liquid droplet that is confined in a rectangular microchannel. The droplet pinching is induced by a local variation of the channel topography and can lead to its break-up. The modification of the channel topography is either induced by a reversible local dilation of the channel bottom wall or by a confinement gradient that is irreversibly modelled in the channel. Interestingly, in both cases, a few micrometres contraction of the channel height leads to the pinching of the droplet in the direction of the channel width. If this pinching is such that the droplet is no longer confined at the level of its deformation, *i.e.* the liquid thread becomes 3D, the droplet splits in two. By minimizing the surface energy of the droplet under the channel confinement gradient, we are able to predict its pinching or its break-up, if any. The dynamic of the droplet deformation is then captured by a semi-analytical model, assuming that most of the viscous dissipation is located in the gutters at the four corners of the channel. Conversely, we show that this kinetic model can be used to extract the average topographic variation of the channel, down to few micrometers, by measuring the droplet pinching dynamics under a classical optical microscope.

## INTRODUCTION

The microfluidic field has thrived over the last decades with the promise of miniaturizing chemical and biological assays to reduce their costs and enhance their throughput [1]. Droplet-based microfluidic platforms are composed of a network of micrometric channels in which water-in-oil or oil-in-water droplets are generated and used as biochemical reactors alternatively to microlitre plates. For such use, it is critical to control the droplet size, monodispersity and frequency generation which are inevitably related to break-up or coalescence events [2].

Droplet breakup is a basic functionality that is required in emulsion science for droplet production. The fragmentation mechanism has been extensively studied in the literature. In the late 19th century, Plateau and Rayleigh showed that droplets of controlled volume can be produced as the result of the destabilization of a liquid thread in an infinite media to minimize its area-to-volume ratio at constant volume [3, 4]. Contrary to droplets in an infinite medium, the geometrical confinement of droplets by walls in microfluidic systems tends to stabilize the liquid thread [5–7], except when Marangoni flows come into play [8].

In microfluidics, there are a large number of techniques to produce droplets at the junction between the two immiscible phases, either by a passive method (T or Y junctions [9–12], flow focusing devices [13–15], step channels [16–18] and confinement gradients [19–21]) or assisted by an active method [22] such as electric field [23], magnetic field [24], or centrifugal forces [25]. Once produced, it is critical to be able to control *in situ* their breakup, in order to produce two daughter droplets from a mother droplet at will. Most of the configurations listed in the literature concern so-called passive systems, in which breakup is associated with a modification of the microchannel geometry (for instance, T or Y junctions leading to two downstream channels [10, 11, 26, 27], or obstacles [28–30]). However, it would be interesting to be able to break the droplets actively, for instance by modifying on-demand and locally the channel geometry. Up to our knowledge, no reported system is able to perform such *in situ* active droplet breakup. Our work addresses this issue, notably.

More specifically, in this paper, we investigate the response of an oil droplet subjected to a local confinement gradient in a microfluidic rectangular channel. We focus on droplets that do not wet the channel wall and are surrounded by an aqueous external phase; and study the effect of local confinement gradient on static droplets, *i.e.* the droplets do not travel in the channel and remain approximately centered under the local confinement gradient. The confinement gradient is applied on demand using a network of heating resistances that locally dilate the bottom silicone layer of the chip. In this *active* device, the local temperature increase can lead to both a channel deformation, more precisely a constriction, and to interfacial stresses that result from a surface tension gradient, called Marangoni stresses. To

capture the mechanisms that prevail during droplet deformation, we also study the fate of a droplet in a passive device, where a similar constriction is irreversibly modelled in the channel and no thermal effects are present. The advantage of the first configuration (active and reversible) compared to the second one (passive and irreversible) is that it can generate a custom deformation. On the other hand, in the second passive device, the droplet pinching is purely mechanical and the channel shape is well-characterized.

The parallel study of the two configurations allows us to determine precisely which mechanism, thickness gradient or Marangoni effect, is ultimately responsible for the droplet breakup in the active device. We find that, in both configurations, the droplet pinches, forming a neck in the observation plane, to counterbalance the increase in its curvature under the local thickness gradient. When the neck forms, the outer phase drains through the four gutters located in between the drop and the corners of the rectangular channel, by mass conservation. The droplet deformation is thus capillary-driven and mediated by the viscous dissipation of the flow in the gutters. Beyond a critical thickness gradient, droplets end up breaking. In our setups, it is important to note that there is no need for a forced flow of the external phase to trigger the droplet breakup.

In the following, we first characterize experimentally the pinching and breakup dynamics and show that in both microfluidic devices, a small local variation of the channel height - 10 to 20 % of the initial channel height - can induce a significant droplet pinching and even lead to its break-up when the confinement gradient is sufficiently large. We then study the droplet pinching and fate theoretically, through the combination of a minimal model relying on surface energy minimisation and *Surface Evolver* numerical simulations [31]. We also propose a power balance between the viscous dissipation and the capillary driving force to capture the time evolution of the droplet deformation. Finally, we demonstrate that, strikingly, this model can also be used to extrapolate topographical defects of a channel from the observation of droplet pinching dynamics.

## MATERIAL AND METHODS

Droplets are composed of mineral oil (Sigma Aldrich M5904). The external phase is an aqueous solution of sodium dodecyl sulfate (SDS, Merck) at a concentration of  $2.94 \text{ g L}^{-1}$  in deionized water (critical micellar concentration,  $c_{cmc} = 1.92 \text{ g L}^{-1}$ ). As such, the droplet does not wet the substrate and is fully surrounded by the external phase. Fluorescein is added to the solution at  $0.44 \text{ g.L}^{-1}$  to enhance the contrast between the droplet and the outer phase under fluorescence microscopy.

The viscosity of the aqueous solution (outer phase) is  $\eta_w = 10^{-3} \text{ Pa s}$  and the viscosity of the mineral oil (inner phase) is  $\eta_i = 25 \times 10^{-3} \text{ Pa s}$ . The interfacial tension between the inner and the outer phases has been measured by a pendant drop method (Kruss DSA30) and equals  $\gamma = 11.1 \text{ mN m}^{-1}$ .

The microfluidic channel is made of poly(dimethylsiloxane) (PDMS) that is bonded to a glass slide on top of which a 30-micron layer of PDMS has been spin-coated and cured. The bonding is achieved using an oxygen plasma (FemtoScience). Water is injected into the microfluidic channel a few minutes after the plasma exposition to ensure that the PDMS channels remain hydrophilic during the experiments. The oil droplets are generated through a T-junction that is designed at the entrance of the microfluidic device. The flow rates of the oil and the aqueous phase are set by a pressure controller (Fluigent MFCX-Flex) which enables the control of the droplet length. The flow rate of the external phase is monitored at the entrance and the output of the channel in order to be able to maintain the droplet *static* within the channel, *i.e.* located centred at the constriction.

In our experiments, the droplets length  $L$ , along the  $x$  direction, ranges from 500 up to 4000  $\mu\text{m}$ , see FIG. 1. The channel cross-section is rectangular such that the droplet is confined in height and width, see FIG. 1.b.c. The ratio between the channel height  $e$ , along the  $z$  axis, and its width  $W$ , along the  $y$  axis, is of the order 1/10, with  $e$  varying from 20 to 40  $\mu\text{m}$  and  $W$  varying from 200 to 400  $\mu\text{m}$ . In such configuration, the characteristic length of the droplet menisci, as well as that of the gutters that are located at the four corners of the channel and bounded by the droplet interface, scales with the channel height  $e$ , see FIG. 1.a.

Two types of devices have been designed to investigate the droplet's pinching and breakup under a local confinement gradient. In the first device, the channel thickness variation that imposes a confinement gradient on the droplet is irreversibly modelled in the chip. By passively pinching the droplet, this device allows us to determine which mechanism prevails when the droplet deformation is triggered by a constriction that is thermally actuated in the second device, using a heating resistance.

- **The passive (irreversible) pinching device**

The confinement gradient is indented in the brass mold with a precision of approximately 100 nm. To verify

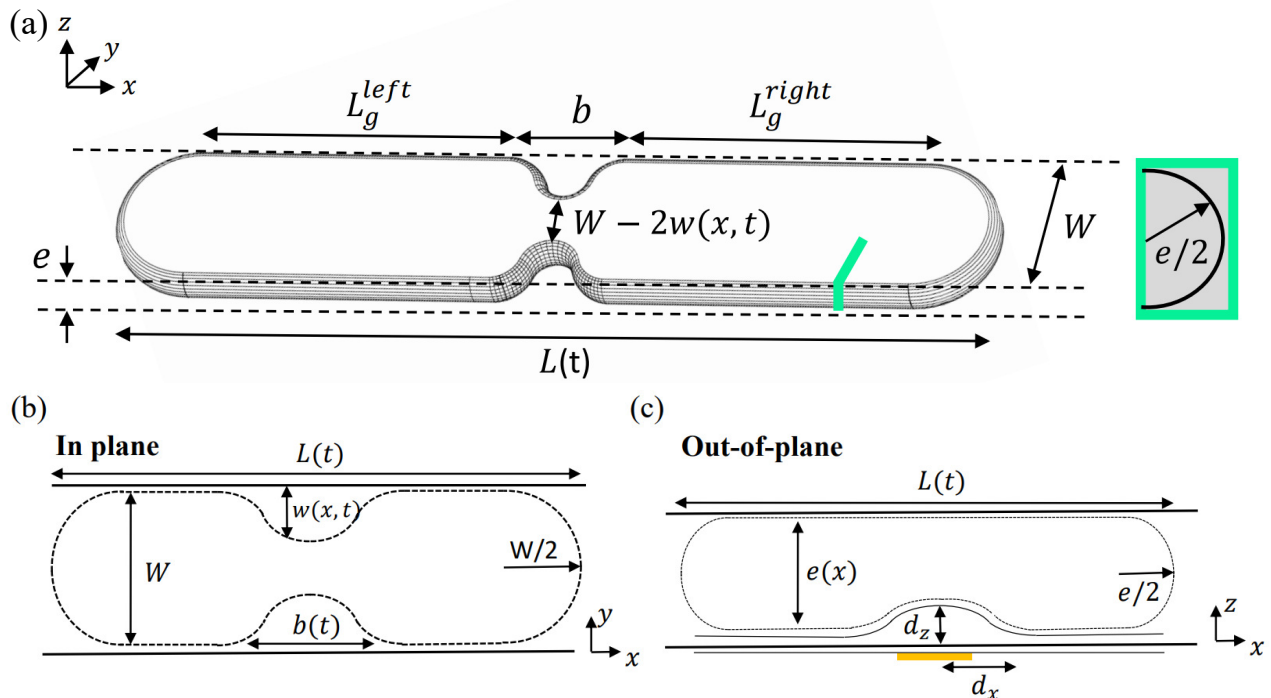


FIG. 1: (a) 3D sketch of the peanut-like deformed droplet confined in the rectangular channel. The green cross-section indicates the gutters' configuration. (b) Sketch of the pinching droplet in the in-plane view, i.e. the observation plane. The droplet deformation is defined by its neck profile  $w(x, t)$ , its width  $b(t)$  and the droplet length  $L(t)$  along the  $x$ -axis. (c) Sketch of the droplet deformation in the out-of-plane, perpendicular to the observation plane. Here, the droplet is deformed by the thermal dilation of the silicone sub-layer of the microfluidic chip (active device), the dimensions of which are  $d_x$  and  $d_y$  along the  $x$ -axis and the  $y$ -axis, respectively.

that the mold has been successfully milled, the indent - characterized by  $d_x$  and  $d_z$  - is observed under a mechanical profilometer. The indentation creates a linear confinement gradient. In the experiments,  $d_x$  varies from 400  $\mu\text{m}$  to 800  $\mu\text{m}$  and  $d_z$  from 3  $\mu\text{m}$  to 10  $\mu\text{m}$ . The tilt angle  $\alpha$  of the confinement gradient is set by the indentation aspect ratio,  $\tan \alpha = d_z/d_x$ , and ranges from 0.2° to 1.4°. The PDMS chip is then replicated from the micromilled brass mold, see FIG. 2.a. The channel thickness variation that results from the constriction is described by  $e(x)$ . In our experiments, the droplet is pushed towards the confinement gradient using pressure controllers and the pressure gradient along the channel is set to zero as soon as the droplet centre reaches the indentation. The droplet starts to deform as soon as it undergoes the confinement gradient. For the purpose of this study, we only focus on the period of time during which the droplet is centred and static under the constriction. This period corresponds to the late times of the droplet deformation (typically the last 40 – 50% of the full droplet deformation process).

#### • The active (reversible) pinching device

The active pinching device is inspired by previous works [32–34]. In this device, the confinement gradient is induced by the thermal dilation of the channel PDMS bottom layer that is located on top of a heating micro-patterned 50  $\mu\text{m}$  wide resistance, see FIG. 2.b. By switching on and off the voltage intensity that is applied to the heating resistance, the confinement gradient is imposed on the droplet on demand. The extent of the channel thickness variation depends on the voltage intensity that is applied to the resistance. Its vertical extent  $d_z$  is characterized using a step microfluidic channel of incremental height, varying from 4 to 10  $\mu\text{m}$ , see FIG. 10.a of Appendix A. For temperatures varying from 55 to 110 °C at the surface of the resistance, the vertical extent  $d_z$  varies between 5  $\mu\text{m} \pm 1 \mu\text{m}$  to 10  $\mu\text{m} \pm 1 \mu\text{m}$ , see FIG. 10.b in Appendix A. The width of the calibration channel is similar to the one of the pinching device. Consequently, the vertical extent  $d_z$  of the confinement gradient can be monitored by adjusting the voltage across the resistance and the horizontal extent  $d_x$  should be approximately equal to the channel width  $W$ , even though it has not been directly characterized. When the voltage is consecutively switched on and off or off and on, the time response of the channel bottom layer dilation is found to be less than 500 ms. As this response is very fast compared to the duration of the droplet pinching,

we consider hereafter that the confinement gradient is imposed or cancelled instantaneously in the channel.

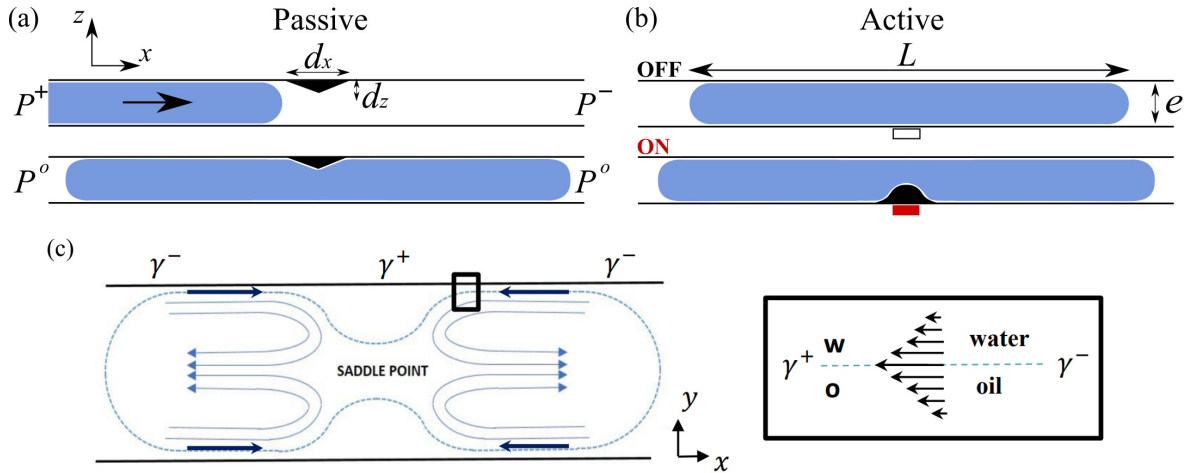


FIG. 2: (a) Side-view of the passive device in which the constriction is already present in the PDMS ceiling (mechanical system). A pressure difference is applied to push and centre the droplet under the constriction, the dimensions of which are  $d_x$  along the  $x$ -axis and  $d_z$  along the  $z$ -axis. (b) Side-view of the active device used to induce on-demand the thermal dilation of the PDMS bottom layer (thermomechanical system). The heating resistance is sketched by the red square. (c) Flows governed by Marangoni thermocapillary gradients at the oil/water interface.

In both devices, the confinement gradient is defined by its horizontal extent  $d_x$  and its vertical extent  $d_z$ , see FIG. 1.b.c. Thus, by taking a reference frame centred at the indentation location, the channel thickness  $e(x)$  can be described as a piecewise function, given by:

$$\begin{cases} \text{for } -\infty \leq x \leq -d_x, & e(x) = e \\ \text{for } -d_x \leq x \leq 0, & e(x) = e - d_z - x d_z/d_x \\ \text{for } 0 \leq x \leq d_x, & e(x) = e - d_z + x d_z/d_x \\ \text{for } d_x \leq x \leq \infty, & e(x) = e \end{cases} \quad (1)$$

In order to quantitatively investigate the droplet pinching, several parameters are introduced, see FIG. 1. The  $(x, y)$  plane corresponds to the in-plane, which is the observation plane, and  $(y, z)$  plane corresponds to the out-of-plane. The droplet length that evolves during pinching is defined as  $L(t)$ . The in-plane distance between the channel wall and the droplet interface, which defines the droplet neck profile along the  $x$ -axis, is defined as  $w(x, t)$ , see FIG. 1.b. The maximum value of this distance, at the centre of the confinement gradient corresponding to  $x = 0$ , is defined as  $w_0(t)$ . Thus, the neck extension along the  $y$ -axis writes  $W - 2w(t)$ , where  $W$  is the channel width, and is defined by  $b(t)$  in the  $x$ -direction. By volume conservation, the neck extension dimensions  $w(x, t)$  and  $b(t)$  can be related to the droplet elongation  $L(t)$ . The droplet deformation is quantified by the spatio-temporal evolution of the neck profile rather than by the droplet length  $L(t)$ . Finally, eight gutters are located between the droplet meniscus and the microfluidic channel corners, see the green box in FIG. 1. The mean gutter length is defined as  $L_g$ . If the droplet is not perfectly centred under the confinement gradient,  $L_g$  is calculated as the equivalent length of the eight gutters placed in parallel next to the droplet neck,  $1/L_g = 1/L_g^{left} + 1/L_g^{right}$ . All these notations are illustrated in FIG. 1.

In addition to the experiments, simulations have been performed using *Surface Evolver* software to compare our observations with predictions given by the minimal surface energy calculation [31].

## OBSERVATIONS AND RESULTS

### Experimental observation of the droplet pinching and breakup

When the droplet undergoes the confinement gradient, it pinches in the  $(x, y)$  plane like a peanut such that a neck forms in its center. The droplet deforms for a few seconds to a few tens of seconds, until it reaches an equilibrium shape or splits into two, see FIG. 3.

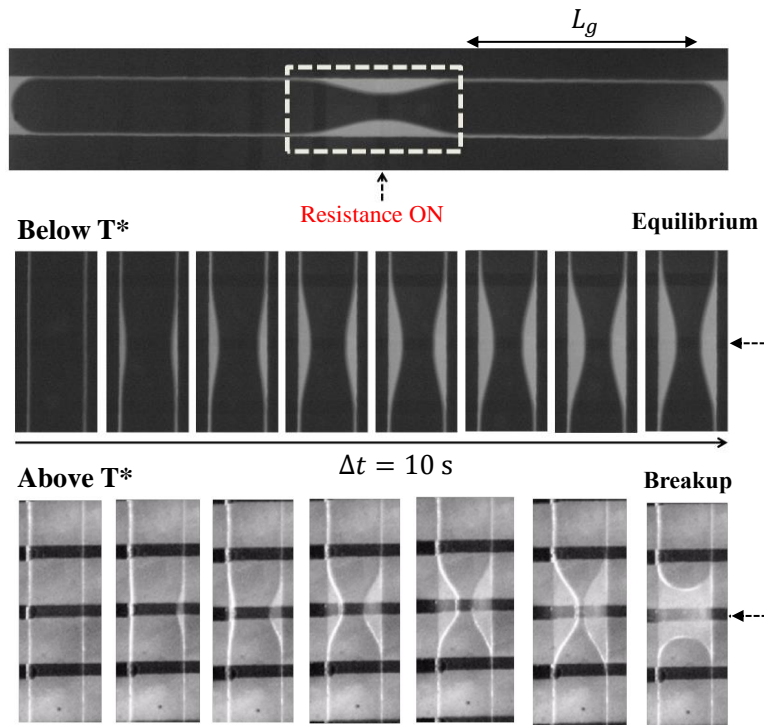


FIG. 3: Active device, snapshots of the droplet deformation in the vicinity of the heating resistance sketched in dashed arrow. A neck forms at the centre of the droplet such that four gutters are present at the corners of the channel, on both sides of the neck. The average gutter length is defined as  $L_g$ . (a) Droplet breakup at  $T=75^\circ\text{C}$  ( $> T^*$ ), (b) Droplet pinching at  $T=55^\circ\text{C}$  ( $< T^*$ ), reaching an equilibrium state. The typical duration of the droplet pinching is a few tens of seconds.

In the active pinching device, the fate of the droplet depends on the maximum temperature increase in the channel. Beyond a certain temperature value  $T^*$ , the droplet deforms until its neck width  $W - 2w_0(t)$  gets smaller than the channel height  $e$ , *i.e.* the droplet neck becomes a three-dimensional thread and then breaks. Conversely, below  $T^*$ , the droplet deforms until it reaches an equilibrium shape in which the neck width is larger than the channel height, *i.e.* the droplet remains confined by the top and bottom walls, see FIG. 3 and FIG. 4. The temperature threshold  $T^*$  delimits the break-up from the non-break-up regime. Figure 4(a) shows the temporal evolution of the neck width at four different temperatures. We see that, at  $47^\circ\text{C}$  and  $50^\circ\text{C}$ , the droplet reaches an equilibrium shape while, at  $60^\circ\text{C}$  and  $68^\circ\text{C}$ , the droplet ends up breaking when its diameter is comparable to the channel height  $e$ , see FIG. 4a & c. At that time, the liquid thread forming the neck switches from a 2D confined shape to a 3D shape where the collapse is always unstable [35, 36]. In the experiment that is illustrated in FIG. 3,  $T^*$  ranges between 60 and  $68^\circ\text{C}$ . While the break-up of the droplet depends on the temperature increase in the vicinity of the resistance, the dynamic of its deformation depends on the initial length of the droplet. The longer the droplet, the more time it takes to deform, see FIG.5 a & b.

In the passive pinching device, the fate of the droplet only depends on the geometrical configuration of the channel. More precisely, the droplet breakup criteria is set by the extent of the channel thickness gradient, defined by  $d_x$  and  $d_y$ . As in the active system, the pinching dynamic of the droplet depends on its length, see FIG.5.a & b.

We now specify how the initial time is defined so that we can carry out a temporal analysis of the fate of the droplets. In the active device, the observation starts when the heating resistance is turned on, see FIG.5.a. In the passive device, the observation time is set as zero when the droplet is approximately centred under the constriction such that four gutters are well located on each side of the droplet, see FIG.5.b. Before  $t_0$ , the droplet is pushed under the constriction and gutters are not well defined, downstream. The droplet deformation can not be easily described. After  $t_0$ , the droplet is no longer pushed in the channel and remains static under the confinement gradient until it breaks, at  $t_f$ . Interestingly, in both devices, the droplet break-up time varies linearly with the gutter length  $L_g$  and with the droplet initial length  $L$ , with an offset corresponding approximately to the neck extension  $b$  along the x-axis, see FIG.5c.



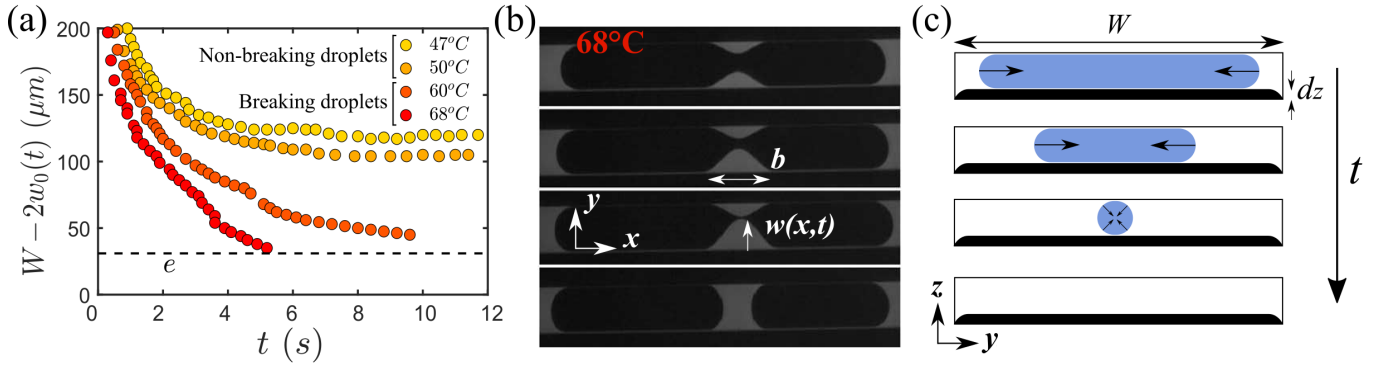


FIG. 4: (a) Time evolution of the neck width,  $W - 2w_0(t)$ , at four different temperatures. At  $47^\circ\text{C}$  and  $50^\circ\text{C}$ , the neck reaches a constant width after a few seconds, signifying that the droplet has reached an equilibrium shape. At  $60^\circ\text{C}$  and  $68^\circ\text{C}$ , the neck width decreases until it reaches the confinement height  $e$  and the droplets break. In these experiments, the channel dimensions are  $e = 30 \mu\text{m}$  and  $W = 200 \mu\text{m}$ . (b) Time-lapse of the droplet deformation and break-up, at  $68^\circ\text{C}$ , in the in-plane. (c) Cross-section sketch of the droplet neck during its pinching at  $x = 0$ . As long as the neck is confined by the channel top and bottom walls, it remains stable. As soon as the neck is no longer confined in the out-of-plane, i.e.  $W - 2w_0 = e$ , it becomes an unstable 3D thread and the droplet splits.

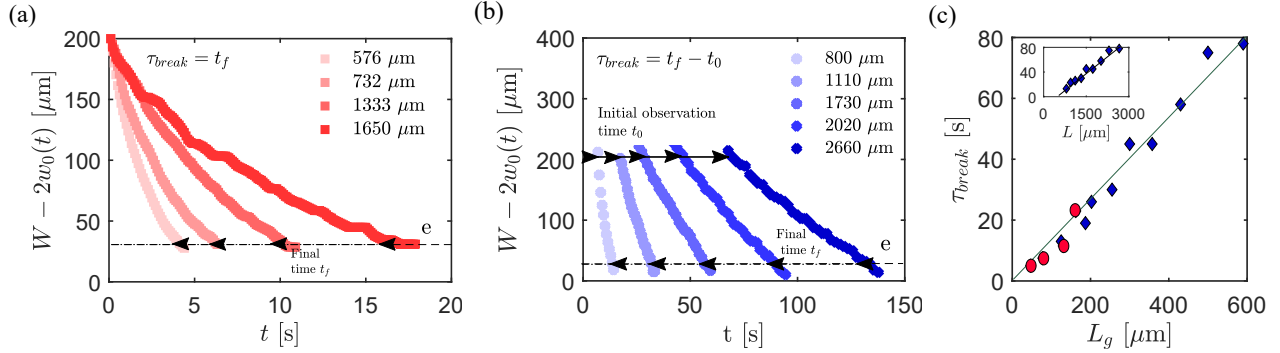


FIG. 5: Time evolution of the neck width  $W - 2w_0$ , for several initial droplet length  $L$ , in both (a) a thermomechanical ( $e = 30 \mu\text{m}$ ,  $W = 200 \mu\text{m}$  and  $T = 60^\circ\text{C}$ ) and (b) a mechanical ( $e = 30 \mu\text{m}$ ,  $W = 400 \mu\text{m}$ ,  $d_x = 400 \mu\text{m}$ , and  $d_z = 5 \mu\text{m}$ , ) system. In both cases, droplets end up breaking, no matter their initial length.  $t_0$  is defined as the initial observation time, after which the droplet remains static under the constriction and the gutters are well defined at each corner of the channel. (c) Evolution of the break-up time versus the equivalent length of the gutters at the four corners of the channel, for the passive device (blue) and the active device (red). In the inset, the break-up time is shown as a function of the initial droplet length.

### Description of the mechanisms for droplet deformation

In the active system, two mechanisms, induced by the local temperature increase, can be responsible for the droplet deformation. The first one is a mechanical effect associated with Laplace pressure gradients, and the second one is a Marangoni effect associated with surface tension gradients, see FIG. 2. The passive device allows us to isolate the first effect.

#### 1/ Mechanical effect

Given that the radius of the droplet meniscus equals  $e/2$  in the out-of-plane dimensions, the channel deformation described by  $e(x)$  leads to a decrease of the local droplet meniscus radius  $e(x)/2$ , see FIG.1.c. The droplet mean curvature writes  $\mathcal{C} = \frac{\partial_x^2 w}{(1 + (\partial_x w)^2)^{3/2}} + \frac{2}{e(x)}$ , where  $\frac{\partial_x^2 w}{(1 + (\partial_x w)^2)^{3/2}}$  is the in-plane curvature [19]. At equilibrium, the Laplace equation sets the curvature to be constant. Therefore, an increase in the droplet out-of-plane curvature, induced by the indentation, must be compensated by a decrease of the in-plane one. At  $t = 0$ , the in-plane curvature of the droplet is zero. The constriction induced by the thermal dilation of the channel in the active device, or by a permanent obstacle in the passive device, is hence counterbalanced by the formation of a neck, the curvature of which

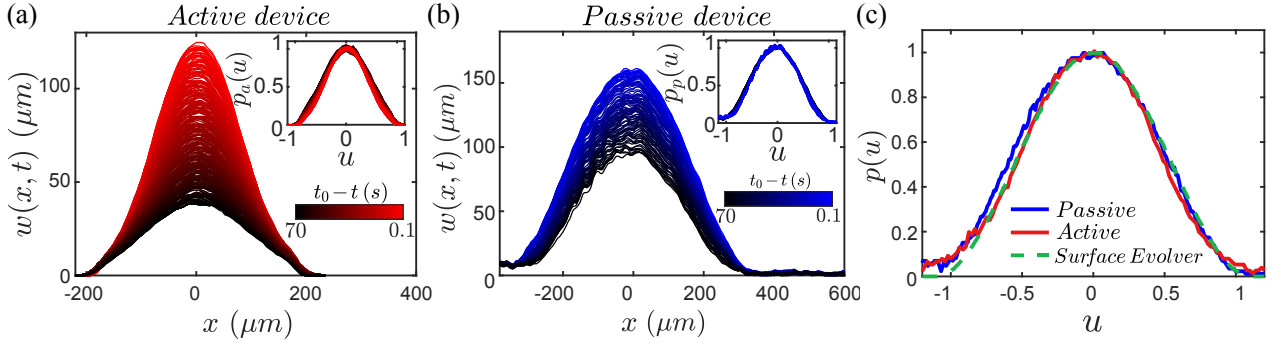


FIG. 6: (a) Time evolution of the neck profile  $w(x,t)$  for an active device ( $W = 400 \mu\text{m}$ ,  $e = 30 \mu\text{m}$  and  $T = 60^\circ\text{C}$ ). The droplet is  $1600 \mu\text{m}$  long. Inset: Collapse of the rescaled profile  $p_a = w/w_0$  versus  $u = x/b$ . (b) Time evolution of the neck profile  $w(x,t)$  for a passive device ( $d_z = 5 \mu\text{m}$ ,  $d_x = 400 \mu\text{m}$ ,  $e = 30 \mu\text{m}$  and  $W = 400 \mu\text{m}$ ). The droplet is  $1600 \mu\text{m}$  long. Inset: Collapse of the rescaled profile  $p_p = w/w_0$  versus  $u = x/b$ . (c) Comparison between the self-similar functions of the Surface Evolver simulations, the active and passive devices,  $p_a$  and  $p_p$ , respectively. The collapse suggests that the same mechanism drives the break-up in both systems, ruling out the contribution of Marangoni effects.

is negative, as described by Dangla *et. al.* [18, 19]. By mass conservation, the outer phase (water) drains towards the centre of the droplet through the gutters to occupy the volume that is released by the formation of this neck. In the meantime, the volume of oil is conserved such that the droplet extremities move slowly away from the constriction. During the whole process, the droplet exhibits a characteristic peanut-like shape, as in FIG. 3.

## 2/ Thermal Marangoni effect (for the active device only)

A surface tension gradient can stem from the local temperature increase in the channel at the level of the heating resistance, see FIG.2.c. In our experimental set-up, the surface tension increase with temperature is equal to  $\partial_T\gamma \sim 2.3 \times 10^{-5} \text{ N.m}^{-1}.\text{K}^{-1}$  while the temperature gradient is typically equal to  $\partial_x T = 10^4 \text{ K.m}^{-1}$  [33]. The Marangoni stress  $\partial_x\gamma = \partial_T\gamma\partial_x T$  that results from these two gradients is thus of the order of  $2 \times 10^{-1} \text{ N.m}^{-2}$ . Being oriented from low to high surface tension regions, Marangoni flows are directed towards the droplet central region where the neck forms. By mass conservation, a saddle point should form in this region, leading the droplet to pinch and eventually break. However, the droplet's ability to sustain an equilibrium shape below  $T^*$ , despite the presence of a temperature gradient, strongly suggests that thermal Marangoni effects are negligible in this study. The hypothesis that only mechanical effects drive the deformation of the droplet is further validated by comparing the active device to the passive one, in which the droplet also displays a steady-state deformation for low indentations and breaks up above a critical threshold.

In a nutshell, in both the mechanical (passive) and the thermomechanical (active) devices, the confinement gradient has to reach a critical value in order to trigger the droplet break-up. Conversely, if this gradient is not sufficient, the droplet deforms until it reaches an equilibrium shape, where the horizontal curvature balances the vertical curvature induced by the deformation, see FIG. 3 & 4.

The droplet pinching dynamic is followed in both devices by measuring the time evolution of the neck profile along the x-axis defined by  $w(x,t)$ , see Figure 6. Interestingly, the extension of the neck along the y-axis, defined by  $b(t)$ , is constant over time and is equal to the horizontal extent of the confinement gradient  $d_x$ . By judiciously rescaling the spatiotemporal evolution of the droplet deformation in both devices, we find that it is self-similar over time [33, 37], see FIG.6. The neck profile is thus described by a self-similar function of the form  $w(x,t) = w_0(t)p(u)$ , with  $u = x/b$  and  $b$  a constant. The insets in FIG. 6a & b display the functions  $p_a$  and  $p_p$  for the active and the passive devices, respectively. These functions collapse on the profile that was obtained by simulating the equilibrium shapes of a droplet placed in similar constrained geometries using the Surface Evolver software, see FIG. 6c. The good agreement between the experimental profiles,  $p_a$  and  $p_b$ , and the one simulated *in-silico* confirms the hypothesis that the droplet is mainly deformed by the confinement gradient that is imposed in the channel. The other mechanisms, such as the thermal Marangoni effect, that can come into play in the active device, will be disregarded subsequently, even at such high temperature gradients ( $\partial_x T \sim 10^4 \text{ k.m}^{-1}$ ).

The droplet breakup occurs when the neck starts to be 3D, *i.e.* when  $W - 2w_0(t) \sim e$ , in agreement with previous studies [35, 36].

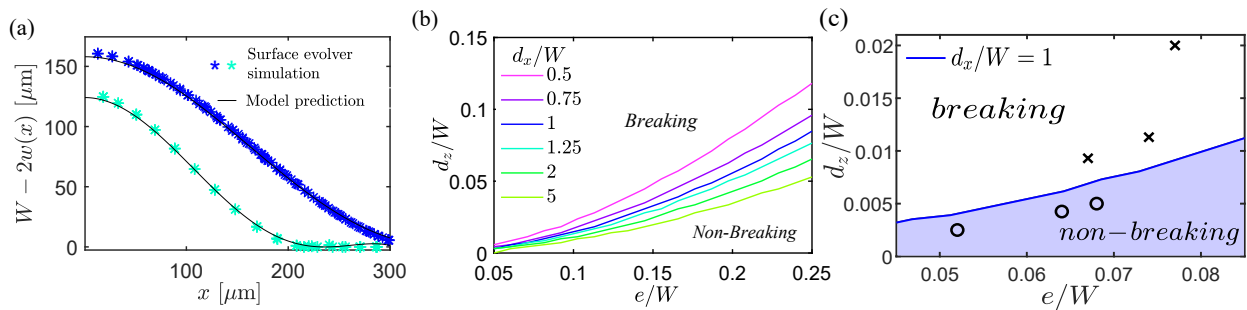


FIG. 7: (a) Comparison between a droplet profile predicted by Surface evolver simulations and by our model, for two sets of channel geometries ( $d_z = 4 \mu\text{m}$ ,  $d_x = 400 \mu\text{m}$ ,  $e = 35 \mu\text{m}$  and  $W = 400 \mu\text{m}$  (blue) and  $d_z = 9 \mu\text{m}$ ,  $d_x = 300 \mu\text{m}$ ,  $e = 40 \mu\text{m}$  and  $W = 200 \mu\text{m}$  (green)). (b) Break-up criteria derived from our calculations for different sets of geometrical parameters ( $e$ ,  $W$ ,  $d_z$ ,  $d_x$ ). The parameters are normalized by the channel width  $W$ . The curves correspond to the spectrum of equations  $W - 2w_0(t_f) = e$ , calculated for several ratios  $d_x/W$ . (c) Comparison between the theoretical predictions and the experiments for six mechanical devices, with  $W$  varying from  $200 \mu\text{m}$  to  $400 \mu\text{m}$ ,  $e$  varying from  $20 \mu\text{m}$  to  $40 \mu\text{m}$ ,  $d_x$  from  $400 \mu\text{m}$  to  $800 \mu\text{m}$  and  $d_z$  from  $3 \mu\text{m}$  to  $10 \mu\text{m}$ .

### Interpretation and model for the final shape of the droplet

In this section, we propose a simple analytical model to predict the final equilibrium shape of the droplet or its breakup, given the geometrical constraints of the channel. Consistently with our above analysis of the driving mechanisms, our model assumes that the droplet deformation is driven by surface energy minimisation under the local confinement gradient.

The final state of a droplet undergoing a mechanical deformation is set by the following criterion:

- the droplet reaches a stable, peanut-like shape when the neck is thicker than the channel height,  $W - 2w_0(t_{eq}) > e$  with  $t_{eq}$  is the time at which the system reaches equilibrium, and
- the droplet breaks when the neck becomes thinner than the channel height at any time  $t$ ,  $W - 2w_0(t) \leq e$ .

The surface energy of the droplet writes  $E = \gamma S$  where  $S$  is its surface area and the surface tension  $\gamma$  is assumed to be constant over time. The excess surface of the droplet, defined as  $\Delta S(t)$ , corresponds to the difference between the surface area of the droplet subjected to the confinement gradient (peanut-like shape) and its initial surface area in the undeformed channel (plug-like shape). We compute  $\Delta S(t)$  as a function of the local variation of the channel height  $e(x)$ , relying on mass conservation to obtain the variation of the droplet length  $\Delta L$ , see Appendix C for more details. At any given time  $t$ , the total surface variation of the droplet writes

$$\Delta S(t) = 4 \int_0^b \left[ \pi e(x) \left( \sqrt{1 + \partial_x w^2} - 1 \right) \left( 1 + \frac{\lambda e(x)}{4} \right) - w(x, t) \left( 1 + \frac{1}{\cos \alpha} + 2\lambda \frac{e(x)}{e} \right) \right] dx \quad (2)$$

where  $\lambda = \frac{W + (\frac{\pi}{2} - 1)e}{W + (\frac{\pi}{4} - 1)e}$  is a geometric parameter of the unindented channel that verifies  $1 < \lambda < 2$ .

We now use our finding that the neck profile is self-similar, that is  $w(x, t) = w_0(t)p(x/b)$ , to write  $\Delta S$  as a function of 6 geometrical parameters,

- the neck extension, defined by its minimal width  $W - 2w_0$  and its extension  $b$
- the channel size, with width  $W$  and height  $e$  and
- the dimensions of the triangular constriction,  $d_x$  and  $d_z$ ,

and the dimensionless function  $p$  and its derivative  $p'$ , obtained from a polynomial fit to the experimental and numerical profiles, see FIG. 6. Details are provided in Appendix D.

By numerically minimizing the excess surface of the droplet  $\Delta S$ , we then predict the equilibrium shape of the droplet, characterised by the equilibrium dimensions of the neck,  $W - 2w_0(t_{eq})$  and  $b$ . We then validate the predictions of  $b$  and  $w_0(t_{eq})$  from our semi-analytical model using *Surface Evolver* simulations and find an excellent agreement for different channel geometries, see FIG. 7.a.

Using the above breakup criterion,  $W - w_0(t_{eq}) < e$ , we now can build a phase diagram based on the dimensionless parameters,  $d_z/W$ ,  $d_x/W$  and  $e/W$ , to predict the fate of the droplet in a wide range of channel geometries, see FIG. 7.b. We compare these predictions to the results of our mechanical passive devices, for which we have access to



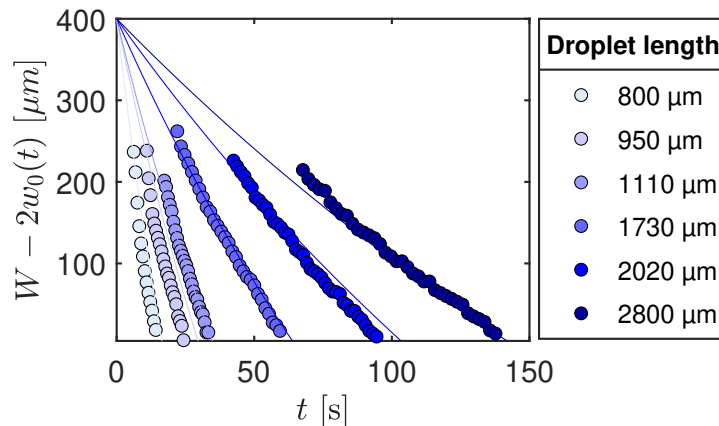


FIG. 8: Time evolution of the neck width  $W - 2w_0(t)$ , for several initial droplet length  $L$ , in a mechanical device ( $d_x = 400 \mu\text{m}$ ,  $d_z = 5 \mu\text{m}$ ,  $e = 30 \mu\text{m}$  and  $W = 400 \mu\text{m}$ ). The experimental data is fitted with our predictive model ( $K = 2.1 \times 10^3$ ).

the exact dimensions of the deformation. All the passive devices designed for this study perform in agreement with our predictions, see FIG. 7.c.

For the active thermomechanical device, we do not have access to the horizontal extent  $d_x$  of the channel thermal dilation with sufficient prediction to assess the performance of this equilibrium, steady prediction. However, we now show that coupling these steady predictions to a dynamical model for the deformation allows us not only to quantify the droplet behaviour in both devices but also to recover the indentation size in active devices.

### Dynamics of the droplet deformation

The droplet pinching is driven by surface energy minimisation but is limited by the viscous dissipation in the droplet oil phase and in the external aqueous phase. The linear increase of the break-up time  $\tau_{break}$  with the gutters length  $L_g$  suggests that the viscous dissipation is mainly located in the gutters, even though the viscosity of the outer phase is smaller than the viscosity of the inner phase ( $\eta_i/\eta_w = 25$ ). Moreover, it is interesting to note that the time evolution of the droplet pinching, displayed in Figure 5.a & b, is radically different from the typical time power-law that governs the evolution of unstable non-confined liquid threads [38].

To model the droplet pinching dynamic, we write a power balance that compares the viscous dissipation power  $\mathcal{P}_g$  with the droplet surface energy increase per unit of time,  $\mathcal{P}_\Sigma = \gamma \partial_t(\Delta S)$ , with  $\Delta S$  given in eq. (2). The rate of change in the droplet surface area can be written as  $\partial_t(\Delta S) = \partial_t w_0 \mathcal{I}(w_0)$ , with  $\mathcal{I}$  an integral that has the dimension of a length and depends on the geometrical parameters of the neck and of the channel.

On the other hand, the viscous dissipation scales as  $\mathcal{P}_g \sim \eta_w \frac{v^2}{e^2} L_g$ , where  $v$  is the typical velocity of the outer phase in the gutters,  $\eta_w v/e$  is the order of magnitude of the shear stress in the gutters and  $e^2 L_g$  is the approximate estimation of the gutter volume. The flow velocity in the gutters  $v$  can be assessed by mass conservation,  $v \sim \frac{1}{e^2} \partial_t \Omega_3$ , with  $\Omega_3$  the volume of water entering the neck region as it forms (see Appendix C). As a result, the viscous dissipation power can be written as  $\mathcal{P}_g = K \frac{\eta_w L_g}{e^4} \mathcal{I}(w_0) (\partial_t w_0)^2$ , where  $\mathcal{I}$  is an integral function that depends on  $w_0$  and on the channel geometry and has the dimension of a surface squared. The dimensionless prefactor  $K$  stands for a permeability constant that takes into account the complexity of the flow in the gutters, including a no-slip velocity at the walls, the tangential stress continuity at the fluid/fluid interface and the complex geometry of the gutter.

Finally, the power balance allows us to write the following differential equation that governs the time evolution of the neck extension  $w_0(t)$ ,

$$\partial_t w_0 = K \frac{\eta_w L_g}{\gamma e^4} \frac{\mathcal{I}(w_0)}{\mathcal{I}(w_0)}. \quad (3)$$

Equation (3) is solved numerically, and the adjustable parameter  $K$  is set by fitting the theoretical time evolution of the neck width  $W - 2w_0(t)$  to the experimental data from the passive device, for which the geometric parameters  $d_x$ ,  $d_z$ ,  $W$  and  $e$  are well characterized, see FIG.8. We find that  $K = 2.1 \times 10^3$ , independently of the droplet length.

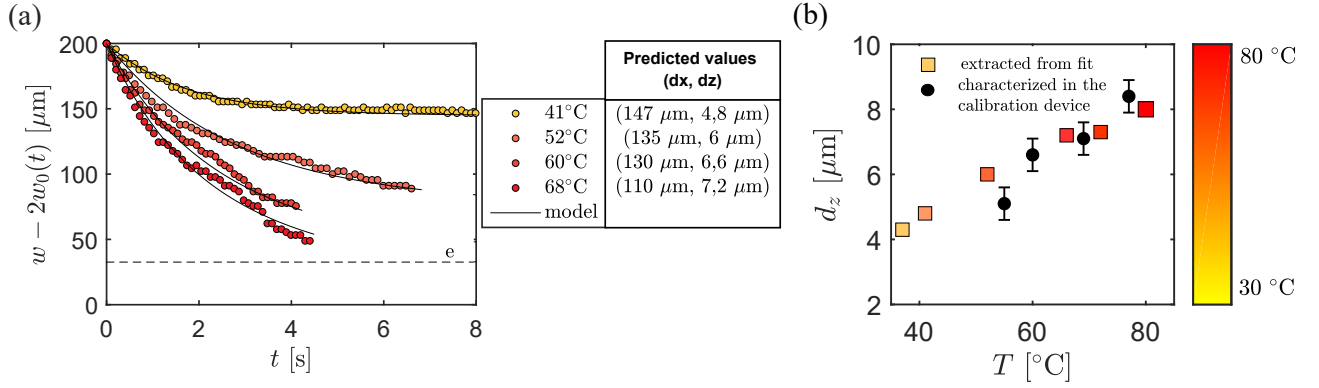


FIG. 9: (a) Fit of the experimental profile of the neck width ( $W - 2w_0(t)$ ) by our model, in order to determine the channel constriction dimensions ( $d_x, d_z$ ) of an active device ( $e = 30 \mu\text{m}$  and  $W = 200 \mu\text{m}$ ), at several temperatures. (b) Comparison between the  $d_z$  values from the fit and the  $d_z$  values extracted from the calibration device, see appendix A.

Strikingly, by setting the permeability  $K$  to the same value  $K = 2.1 \cdot 10^{-3}$ , the model conversely allows us to probe the channel topography in the active device. As a reminder, in this device, the vertical extent of the constriction  $d_z$  has been characterized as a function of the maximum temperature increase in the channel, while its horizontal extent  $d_x$  remains unknown. To determine  $d_x$  from the above model, we define the dimensionless function  $N$  that calculates the difference between the theoretical and the experimental time evolution of the neck profile,  $w_{th}$  and  $w_{exp}$ , respectively.  $N$  is defined as  $N(d_x, d_z) = 4[w_{xp}(t) - w_{th}(t)]^2 / e_{rr}^2$ , with  $e_{rr}$  being the typical error of the image processing, which is considered to be twice the pixel size, approximately equal to  $10 \mu\text{m}$ . The extent of the topographic variation induced by the thermal dilation of the channel walls in the active device,  $d_x$  and  $d_z$ , is calculated by minimizing the function  $N$ . The prediction of  $d_x$  and  $d_z$ , for four sets of experimental data, is illustrated in FIG.9.a. The predicted values for  $d_z$  are in good agreement with the  $d_z$  values that were characterized using the calibration device described in Appendix A, see FIG.9.b. Unfortunately, we are not able to verify the  $d_x$  values since they have not been properly characterized. Surprisingly, they seem to decrease with temperature, which might be related to the mechanical response of the silicone layer to high local thermal stresses. Such a response to high thermomechanical stress is out of the scope of this paper. Moreover, it is interesting to note that the sensitivity of  $N$  to small variations in  $d_x$  and  $d_z$  is high, indicating that the model should be able to detect out-of-plane defects on the order of hundreds of nanometers, which are tens of micrometres large in the in-plane, see appendix F. More generally, we believe that observing the time evolution of in-plane droplet pinching can reveal small topographic defects in microfluidic channels, which are difficult to measure with optical techniques but can be quantified using our model.

## CONCLUSION

In this paper, we present a novel thermomechanical system that allows for an in situ break-up of droplets in microfluidic rectangular channels due to local variation of the channel topography. This topography change is induced by micropatterned resistances that locally heat and expand the silicone layer, coated on the glass slide of the microfluidic chip. Strikingly, we find that even small deformations in the channel geometry can lead to large reversible deformations of the droplet or a breakup, providing a controlled and practical mechanism for selectively breaking a droplet after it has been formed.

We study experimentally and theoretically the precise mechanism for droplet breakup and quantify the threshold between reversible deformation and breakup. We investigate the behaviour of a non-wetting droplet, confined in a rectangular channel, with a resistance. When the resistance is turned on, the PDMS is locally swollen, leading to mechanical deformation of the channel and drop, and the local fluids heat up, leading to local temperature gradients and corresponding Marangoni effects. For weak deformations, we find that the droplet maintains its equilibrium steady shape, even under continuous heating. This suggests that our system is dominated by mechanical deformation with a negligible contribution of the thermal surface tension gradients. Accordingly, a second passive device that mimics the channel thickness variation induced by the thermal dilation of the channel walls in the thermomechanical device has the same dynamics as the active thermomechanical device, except that the constriction size and the fate of the droplet cannot be controlled.

We can therefore propose a minimal, semi-analytical model for the droplet dynamics and final state focusing on mechanical effects and surface minimisation. We show that in both devices, the fate of the droplet is determined by a global surface energy minimisation. The neck size is set by the channel geometry and the extent of the confinement gradient. If the neck size that minimises the surface energy is wider than the channel height, the droplet reaches an equilibrium steady-state configuration. If the neck is thinner than the channel width, the droplet breaks. We can therefore predict the fate of the droplet for a given geometry using direct *Surface Evolver* simulations or a minimal model that relies on the self-similarity of the neck shape. The dynamics of the deformation and breakup are instead set by the length of the gutters at the four channel corners. We model the time evolution of the deformation by balancing the rate of change in the droplet surface area with the viscous dissipation power in the gutters, using an adjustable parameter  $K$  that accounts for the permeability in the gutters. Our predictions, with a single parameter, are validated in both the thermomechanical and purely mechanical devices.

Conversely, our predictive model can be used to quantify in situ out-of-plane topographic defects in a microfluidic channel theoretically down to a few hundred nanometers, which are challenging to measure with conventional microscopic or profilometric techniques. Furthermore, we believe that the thermomechanical device that was used for this study and that is inspired by previous work [32] can add a new, well-controlled, on-demand breakage function to the range of features explored in droplet microfluidics.

### ACKNOWLEDGEMENTS

This work was supported by Centre National de la Recherche Scientifique (CNRS), ESPCI Paris, Université de Rennes and the Agence Nationale de la Recherche (ANR) under Grant No. ANR-18-CE09-0029, IPGG (Equipex ANR-10- EQPX-34 and Labex ANR-10-LABX-31), PSL (Idex ANR-10-IDEX-0001-02). AT is grateful to the Simons Foundation through the Math + X grant awarded to the University of Pennsylvania where part of the modelisation has been performed.

---

\* Electronic address: [marie-caroline.jullien@univ-rennes.fr](mailto:marie-caroline.jullien@univ-rennes.fr)

- [1] P. Tabeling, *Introduction to microfluidics* (OUP Oxford, 2005).
- [2] C. N. Baroud, F. Gallaire, and R. Dangla, *Lab on a Chip* **10**, 2032 (2010).
- [3] J. A. F. Plateau, *Statique expérimentale et théorique des liquides soumis aux seules forces moléculaires*, vol. 2 (Gauthier-Villars, 1873).
- [4] J. W. Strutt and L. Rayleigh, *Proc. London Math. Soc* **10** (1878).
- [5] P. Guillot, A. Colin, A. S. Utada, and A. Ajdari, *Physical review letters* **99**, 104502 (2007).
- [6] P. Guillot, A. Colin, and A. Ajdari, *Physical Review E* **78**, 016307 (2008).
- [7] M. Cabezas, M. Herrada, and J. M. Montanero, *Physical Review E* **100**, 053104 (2019).
- [8] M. Clerget, A. Klimenko, M. Bourrel, F. Lequeux, and P. Panizza, *Physics of Fluids* **35** (2023).
- [9] P. Garstecki, M. J. Fuerstman, H. A. Stone, and G. M. Whitesides, *Lab on a Chip* **6**, 437 (2006).
- [10] L. Ménétrier-Deremble and P. Tabeling, *Physical Review E—Statistical, Nonlinear, and Soft Matter Physics* **74**, 035303 (2006).
- [11] M.-C. Jullien, M.-J. Tsang Mui Ching, C. Cohen, L. Menetrier, and P. Tabeling, *Physics of Fluids* **21**, 072001 (2009).
- [12] A. Leshansky, S. Afkhami, M.-C. Jullien, and P. Tabeling, *Physical review letters* **108**, 264502 (2012).
- [13] S. L. Anna, N. Bontoux, and H. A. Stone, *Applied physics letters* **82**, 364 (2003).
- [14] S. Takeuchi, P. Garstecki, D. B. Weibel, and G. M. Whitesides, *Advanced materials* **17**, 1067 (2005).
- [15] A. Dewandre, J. Rivero-Rodriguez, Y. Vitry, B. Sobac, and B. Scheid, *Scientific reports* **10**, 1 (2020).
- [16] S. Barkley, E. R. Weeks, and K. Dalnoki-Veress, *The European Physical Journal E* **38**, 1 (2015).
- [17] A. Montessori, M. Lauricella, S. Succi, E. Stolovicki, and D. Weitz, *Physical Review Fluids* **3**, 072202 (2018).
- [18] R. Dangla, E. Fradet, Y. Lopez, and C. N. Baroud, *Journal of Physics D: Applied Physics* **46**, 114003 (2013).
- [19] R. Dangla, S. C. Kayi, and C. N. Baroud, *Proceedings of the National Academy of Sciences* **110**, 853 (2013).
- [20] L. Keiser, R. Herbaut, J. Bico, and E. Reyssat, *Journal of Fluid Mechanics* **790**, 619 (2016).
- [21] N. Taccoen, B. Dollet, and C. N. Baroud, *Physical review letters* **123**, 238006 (2019).
- [22] P. Zhu and L. Wang, *Lab on a Chip* **17**, 34 (2017).
- [23] P. He, H. Kim, D. Luo, M. Marquez, and Z. Cheng, *Applied Physics Letters* **96** (2010).
- [24] Y. Wu, T. Fu, Y. Ma, and H. Z. Li, *Soft Matter* **9**, 9792 (2013).
- [25] S. Haeberle, R. Zengerle, and J. Dürée, *Microfluidics and Nanofluidics* **3**, 65 (2007).
- [26] J. Zhou, Y.-M. Ducimetière, D. Migliozi, L. Keiser, A. Bertsch, F. Gallaire, and P. Renaud, *Physical Review Fluids* **8**, 054201 (2023).
- [27] P. Cochard-Marchewka, N. Bremond, and J. Baudry, *Lab on a Chip* **23**, 2276 (2023).

- [28] A. Nishimura, A. Schmit, L. Salkin, L. Courbin, and P. Panizza, *Microfluidics and Nanofluidics* **21**, 94 (2017).  
 [29] Z. Li, Z. Gu, R. Li, C. Wang, C. Chen, C. Yu, Y. Zhang, Q. Shu, W. Cao, and J. Su, *Physics of Fluids* **34** (2022).  
 [30] L. Salkin, A. Schmit, L. Courbin, and P. Panizza, *Lab on a Chip* **13**, 3022 (2013).  
 [31] K. A. Brakke, *Experimental mathematics* **1**, 141 (1992).  
 [32] V. Miralles, A. Huerre, H. Williams, B. Fourni e, and M.-C. Jullien, *Lab on a Chip* **15**, 2133 (2015).  
 [33] M. Kerdraon, J. D. McGraw, B. Dollet, and M.-C. Jullien, *Physical Review Letters* **123**, 024501 (2019).  
 [34] M. Pascual, M. Kerdraon, Q. Rezard, M.-C. Jullien, and L. Champougny, *Soft Matter* **15**, 9253 (2019).  
 [35] B. Dollet, W. van Hoeve, J.-P. Raven, P. Marmottant, and M. Versluis, *Physical review letters* **100**, 034504 (2008).  
 [36] W. Van Hoeve, B. Dollet, M. Versluis, and D. Lohse, *Physics of fluids* **23**, 092001 (2011).  
 [37] J. D. McGraw, T. Salez, O. B aumchen, E. Rapha el, and K. Dalnoki-Veress, *Physical Review Letters* **109**, 128303 (2012).  
 [38] R. F. Day, E. J. Hinch, and J. R. Lister, *Physical review letters* **80**, 704 (1998).

## APPENDIX

### A-Calibration device for the thermomechanical deformation height.

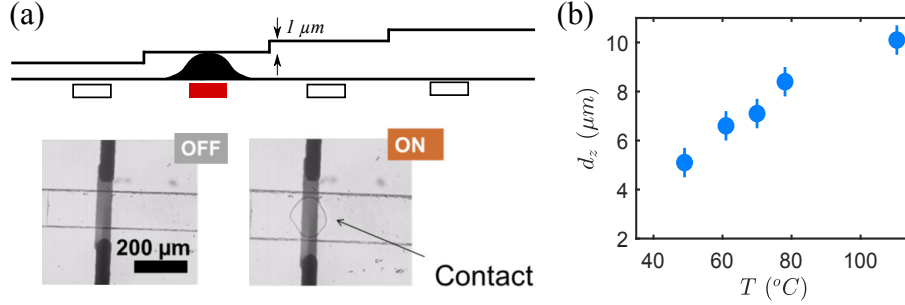


FIG. 10: (a) Sketch of the channel with 1 μm steps, obtained from micromilled brass mold and used to characterize the thermomechanical deformation. The contact zone is directly visible under the microscope. (b) Deformation height  $d_z$  versus the maximum temperature of the heating resistance.

### B-Increase of the interfacial tension with temperature measured by pendant drop method.

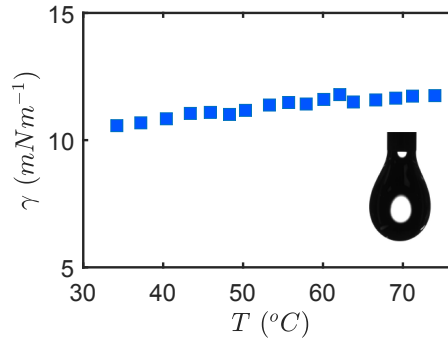


FIG. 11: Interfacial tension as a function of the temperature, measured by the pendant drop method. Inset: picture of a drop of mineral oil in SDS solution.

### C- Detailed calculation of the droplet surface variation.

Here, we estimate the change in surface area that the drop undergoes in the presence of an indentation, that is, the difference between the surface energy of the peanut-shaped deformed droplet at time  $t$  and that of the plug-like,

undeformed one at  $t = 0$ .

Because the droplet is centred at the level of the confinement gradient, the axis  $x = 0$  is an axis of symmetry for the droplet. Hence, we only consider the half-surface of the droplet and we delineate three regions :

- (1) the droplet extremity which only translates in the channel
- (2) the sides of the droplet which are elongated during the evolution and where the gutters are localized
- (3) the confinement gradient region where the neck forms. The extension of the neck in the  $x$ -direction is  $b$ , and its profile is  $w(x, t)$ .

Figure 12 illustrates the regions 1, 2 and 3. We calculate the excess surface of the droplet interface in each of these regions. We note that, because increased confinement leads to Laplace pressure changes, we expect the neck region (3) to span the section of the drop that is over the indentation so that  $b \approx d_x$ . We confirm experimentally that the  $x$ -direction extension of the neck  $b$  is comparable to that of the indentation  $d_x$ , and is constant in time, even as the deformation  $y$ -amplitude grows.

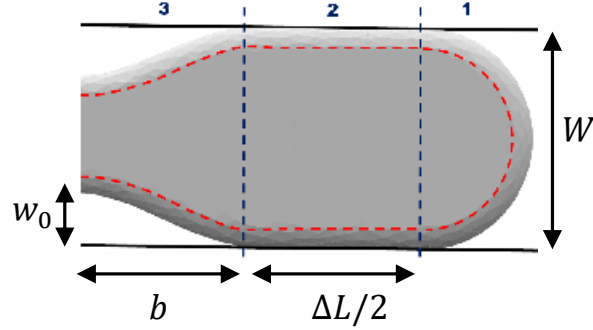


FIG. 12: Regions 1, 2 and 3 for the detailed calculation of  $\Delta S$ .

*Region 1:* The surface of the droplet interface is not modified in this region, which translates in the channel without changing shape.

*Region 2:* In region (2), the confinement height is constant and equal to  $e$ . By mass conservation, as the neck forms, the length of region (2),  $l(t)$ , therefore increases by  $\Delta L/2$ , with  $\Delta L$  the total length increase of the drop.

The total surface change of the region (2) including the menisci is given by

$$\Delta S_2 = \left[ 2(W - e) + 2\pi \frac{e}{2} \right] \Delta L/2, \quad (4)$$

while its volume change is

$$\Delta \Omega_2 = \left[ (W - e)e + \pi \left( \frac{e}{2} \right)^2 \right] \Delta L/2. \quad (5)$$

*Region 3:* The area of region 3 is more intricate to evaluate, as it has a complex shape, set by the confinement height  $e(x)$  and the in-plane distance from the neck to the wall  $w(x, t)$ . We can however evaluate it by recalling that the slope of the indentation is small,  $\alpha \ll 1$  with  $\tan \alpha = \delta x / \delta z$ . We consider separately the changes in surface area of the top surface,  $\Delta S_3^t$ , the bottom one in contact with the indentation,  $\Delta S_3^b$ , and the menisci  $\Delta S_3^m$ .

The top and bottom surfaces are flat. The change in the surface area of the top surface is

$$\begin{aligned} \Delta S_3^t &= \left[ Wb - 2 \int_0^b \left( w(x, t) + \frac{e(x)}{2} \right) dx \right] - [W - e(x)]b \\ &= - \int_0^b 2w(x, t) dx, \end{aligned} \quad (6)$$

while that of the bottom one, which is tilted by an angle  $\alpha$ , is

$$\Delta S_3^b = - \frac{1}{\cos \alpha} \int_0^b 2w(x, t) dx. \quad (7)$$



The shape of the two menisci is set by the local channel height  $e(x)$  and the constant mean curvature of the entire drop. In the limit of small indentations,  $\alpha \ll 1$ , we can approximate it for a given neck shape  $w(x, t)$  by considering small cylindrical sections of radius  $e(x)/2$  and height  $ds$  along the arclength  $s$  of the meniscus. Noting that  $ds = dx\sqrt{1 + (\partial_x w)^2}$ , we get the surface area change

$$\Delta S_3^m = 2 \int_0^b \pi e(x) (\sqrt{1 + \partial_x w^2} - 1) dx. \quad (8)$$

Finally, the total area change in region (3) is

$$\Delta S_3 = -2 \left(1 + \frac{1}{\cos \alpha}\right) \int_0^b w(x, t) dx + 2 \int_0^b \pi e(x) (\sqrt{1 + \partial_x w^2} - 1) dx. \quad (9)$$

Similarly, we obtain the volume change

$$\Delta \Omega_3 = -2 \int_0^b w(x, t) e(x) dx + \frac{\pi}{4} \int_0^b e(x)^2 (\sqrt{1 + \partial_x w^2} - 1) dx. \quad (10)$$

*Mass conservation.* By volume conservation of the droplet,  $\Delta \Omega_2 = \Delta \Omega_3$ , we obtain the elongation of the droplet  $\Delta L$  as

$$\Delta L = 2 \frac{1}{W + (\frac{\pi}{4} - 1) e} \left[ -2 \int_0^b w(x, t) \frac{e(x)}{e} dx + \frac{\pi}{4} \int_0^b \frac{e(x)^2}{e} (\sqrt{1 + \partial_x w^2} - 1) dx \right]. \quad (11)$$

The total surface change of the entire droplet,  $\Delta S$ , is then

$$\Delta S = 4 \int_0^b \left\{ \pi e(x) (\sqrt{1 + \partial_x w^2} - 1) \left[ 1 + \frac{\lambda e(x)}{4e} \right] - w(x, t) \left[ 1 + \frac{1}{\cos \alpha} + 2\lambda \frac{e(x)}{e} \right] \right\} dx, \quad (12)$$

where

$$\lambda = \frac{W + (\frac{\pi}{2} - 1) e}{W + (\frac{\pi}{4} - 1) e} \quad (13)$$

is a geometric parameter of the unindented channel with  $1 < \lambda < 2$ .

We now use the result from our experiments and *Surface Evolver* simulations that the neck profile is self-similar and can be collapsed on a single function  $p(u)$  with  $u \in [-1, 1]$ . We can then write that for  $-b < x < b$ ,  $x = bu$ ,  $w(x, t) = w_0(t)p(u)$  and  $e(x) = e - d_z + d_z \min(1, \frac{b}{d_x}|u|)$ . Denoting for conciseness  $\bar{u} = \min(1, \frac{b}{d_x}|u|)$ ,

$$\begin{aligned} \Delta S(w_0, b) = 4b \int_0^1 \left\{ \pi \left( \sqrt{1 + \left(\frac{w_0}{b}\right)^2 p'(u)^2} - 1 \right) (e - d_z(1 - \bar{u})) \left[ 1 + \frac{\lambda}{4} \left( 1 - \frac{d_z}{e} (1 - \bar{u}) \right) \right] \right. \\ \left. - w_0 p(u) \left[ 1 + (\cos \alpha)^{-1} + 2\lambda \left( 1 - \frac{d_z}{e} (1 - \bar{u}) \right) \right] \right\} du. \end{aligned} \quad (14)$$

The surface area is set by the amplitude of the neck  $w_0$ , its aspect ratio  $w_0/b$ , and the geometry of the channel ( $W$ ,  $e$ ) and the indentation ( $d_x$ ,  $d_z$ ). The equilibrium neck shape ( $w_{eq}$ ,  $b_{eq}$ ) corresponds to the minimum of  $\Delta S$ , which we then obtain numerically using the built-in Matlab function *fminsearch*.

#### D- Polynomial approximation of the self-similarity function for the neck profile

The function  $p$  is extracted from the experimental data. More precisely,  $p$  is obtained by fitting the experimental profiles illustrated in FIG. 6. We find for  $0 < u < 1$ ,

$$p(u) = -1.6727u^5 + 3.3531u^4 + 0.317u^3 - 3.0016u^2 + 0.0033u + 1.0001 \quad (15)$$

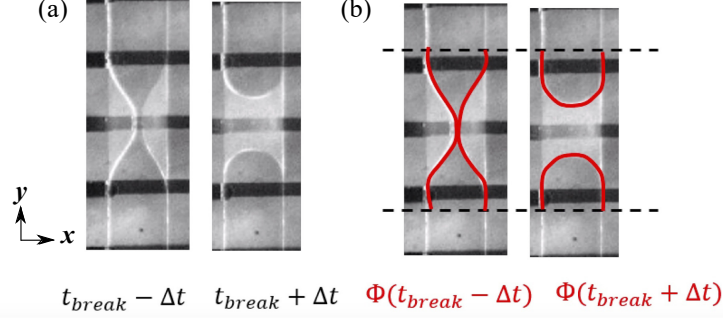


FIG. 13: Calculation of the droplet in-plane interface perimeter at the level of the neck, just before and just after the break-up event ( $\Phi(\tau_{break} - \Delta t) = 512 \mu\text{m}$  and that  $\Phi(\tau_{break} + \Delta t) = 460 \mu\text{m}$ ).

### E- Detailed calculation of the power balance

The neck formation is driven by surface energy minimization of the drop, which is instantaneously compensated by the viscous dissipation from the generated flows. To model the droplet deformation dynamics, we therefore write a power balance that compares the viscous dissipation power with the excess surface energy that is increased in the system per unit of time.

In our system, viscous dissipation occurs in the gutters of the drop as well as the neck region. As the gutters are highly confined, we expect them to dominate the viscous dissipation, which is confirmed by showing that the break-up time in a given geometry scales linearly with the droplet length. We therefore only balance the power from surface area minimization  $\mathcal{P}_\Sigma$  and the viscous dissipation in the gutters  $\mathcal{P}_g$ .

*Viscous dissipation in the gutters* The viscous dissipation power for a flow with velocity  $\mathbf{v}$  in a volume  $\Omega$  is given by

$$\mathcal{P} = \oint_{\Omega} \eta (\nabla v + {}^T \nabla v)^2 d\Omega \quad (16)$$

where  $\eta$  is the viscosity of the fluid. In the gutters, this power scales as

$$\mathcal{P}_g \sim \eta_w \frac{v^2}{e^2} L_g \quad (17)$$

where  $v$  is the characteristic velocity in the gutters. By conservation of mass, the flow rate of water that fills the neck region (3) as the drop deform is equal to the flow rate in the gutters, that is,  $ve^2 \sim \partial_t \Omega_3$ , with  $\Omega_3$  given in (10).

We now introduce a constant dimensionless coefficient  $K$  that accounts for the flow profile in the gutters, independently of the channel geometry, and write

$$\mathcal{P}_g = K \frac{\eta_w L_g}{e^4} [\partial_t \Omega_3]^2. \quad (18)$$

Using the self-similar form of the neck profile  $w(x, t) = w_0(t)p(x/b)$ ,

$$\partial_t \Omega_3 = \partial_t w_0(t) \int_0^1 \left[ -2bp(u)e(bu) + \frac{\pi}{4} \frac{w_0(t)}{b} e(bu)^2 p'(u)^2 \left( 1 + \frac{w_0(t)^2}{b^2} p'(u)^2 \right)^{-3/2} \right] du. \quad (19)$$

Therefore, the viscous dissipation power writes

$$\mathcal{P} = K \frac{\eta_w L_g}{e^4} (\partial_t w_0)^2 \mathcal{I}(w_0), \quad (20)$$

where the integral  $\mathcal{I}$  depends on the next extension and the channel and indentation geometry,

$$\mathcal{I}(w_0) = \left[ \int_0^1 \left( -2bp(u)e(bu) + \frac{\pi}{4} \frac{w_0(t)}{b} e(bu)^2 p'(u)^2 \left( 1 + \frac{w_0(t)^2}{b^2} p'(u)^2 \right)^{-3/2} \right) du \right]^2. \quad (21)$$

*Power from the surface energy minimization* The power from the decrease in surface energy is  $\mathcal{P}_\Sigma = \gamma \partial_t(\Delta S)$ . We obtain the rate of change of the surface area of the drop by deriving eq. (14) with respect to time,

$$\begin{aligned} \partial_t \Delta S &= \partial_t w_0 \int_0^1 4 \left\{ \pi \frac{w_0(t)}{b} p'(u)^2 \left( 1 + \frac{w_0(t)^2}{b^2} p'(u)^2 \right)^{-3/2} e(bu) \left[ 1 + \frac{\lambda}{4} \frac{e(bu)}{e} \right] \right. \\ &\quad \left. - b p(u) \left[ 1 + (\cos \alpha)^{-1} + 2\lambda \frac{e(bu)}{e} \right] \right\} du \\ &= \partial_t w_0 \mathcal{J}(w_0), \end{aligned} \quad (22)$$

with the integral  $\mathcal{J}_0(w_0)$  depending on the channel geometry. Similarly to the case of the viscous dissipation, we therefore write the power from surface energy minimization as

$$\mathcal{P}_\Sigma = \gamma \partial_t w_0 \mathcal{J}(w_0). \quad (23)$$

*Power balance* From the power balance  $\mathcal{P}_\Sigma = \mathcal{P}_g$ , we get that

$$\partial_t w_0 = \frac{K \eta_w L_g}{\gamma e^4} \frac{\mathcal{I}(w_0)}{\mathcal{J}(w_0)}. \quad (24)$$

We can solve this equation numerically using a forward Euler method, starting from the undeformed droplet  $w_0(0) = 0$  as an initial condition. The adjustable parameter for the gutter flow  $K$  is set by fitting this prediction for the neck dynamics  $w_0(t)$  to the experimental data from the mechanical devices, in which the geometric parameters ( $d_x$ ,  $d_z$ ,  $W$  and  $e$ ) are well characterized, and obtain that  $K = 2.1 \times 10^{-3}$ .

#### F- Sensitivity of the error function $N$ to small variations near the best fitting values of $(d_x, d_z)$ .

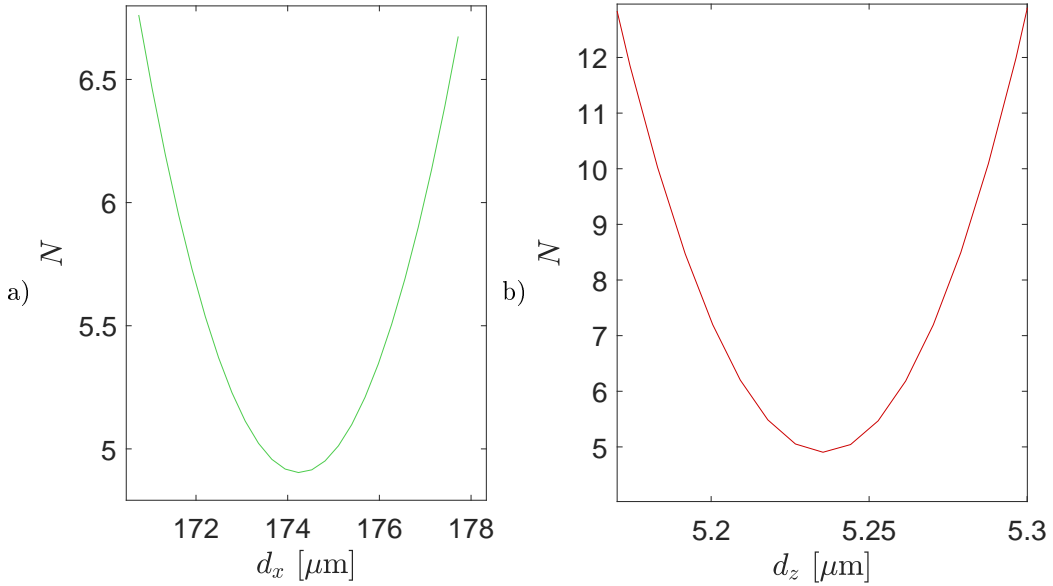


FIG. 14: Evolution of the error function  $N$  as a function of  $d_x$  (a) and  $d_z$  (b) small variations near the best fitting values ( $d_x$ ,  $d_z$ ) shown in FIG.9.